preprint Energy & Fuels

Received 31 October 2020,
Accepted 20 December 2020
https://doi.org/10.1021/acs.energyfuels.0c03662

preprint for final article published: *Energy & Fuels, 35, 1874-1884 (2021)*

Thermodynamic barrier to nucleation for manganese oxide nanoparticles synthesized by high-temperature gas-to-particle conversion

Shruthi Dasappa[a,b] and Joaquin Camacho [*a]

A complementary experimental and modeling study is reported here for nucleation of manganese oxide nanoparticles in premixed stagnation flames. The current synthesis occurs at relatively high flame temperature and low precursor loading. Thermodynamic analysis based on the postulated nucleation process, Mn(g) + O2(g) MnO(s), is carried out to quantify precursor supersaturation and potential impacts of the Kelvin effect on particle formation. Nucleation and growth are analyzed based on the computed temperature-time-oxygen history in the post-flame region. Agreement between measured and computed flame position for the base flame and precursor doped flames indicates that the manganese methylcyclopentadienyl tricarbonyl precursor does not inhibit flame chemistry for the conditions currently studied. Particle size distributions measured by mobility particle sizing and TEM images show reasonable agreement. Moreover, the measured particle size is predicted much more closely by a nucleation-limited mechanism rather than the size predicted by coagulation-limited growth.

Introduction

Flame-based processes enable precise and scalable production of functional nanomaterials [1–3]. Advantages of flame synthesis routes over wet-chemistry include less synthesis steps, much faster conversion and continuous production [1]. Several flame configurations have proven useful for tailoring material properties of nano-scale products including carbon (graphene, nanotubes) [4–6], metals [7,8] and metal oxides [9–12]. Premixed stagnation flames are employed in the current study to provide a one-dimensional growth process for isolation of the manganese oxide nucleation process under a well-characterized temperature-time history. Relatively high flame temperatures are achieved in premixed stagnation flames and previous works using these flames focused on phase stability of TiO2 [13,14] and manganese oxides [15,16] at high temperature (T > 2200 K). This particular flame synthesis method is amenable to fundamental studies of gas-to-particle conversion as well as application to film deposition processes for fabrication of functional films [17]. Nano-scale manganese oxide is a promising material for medical imaging [18], catalysis [19], and energy storage [20]. In principle, the films formed here and in previous work have the potential to serve as energy storage electrodes or catalysts. Insight into competing processes gained from premixed stagnation flame studies could also be applied to design more complex, yet scaled up processes such as flame spray synthesis.

We have previously shown that temperature and oxygen growth conditions could be manipulated to produce manganese oxide nanoparticles in flames with some selectivity in the oxidation state and nano-structure [15,16]. Phase equilibria among MnO, Mn_3O_4, Mn_2O_3 and MnO_2 largely governs the final product formed while cooling and coagulation rates also contribute to the final product properties. The range of valences observed in stable products of manganese oxide is wider than has been reported for flame synthesized TiO2 and Fe2O3. This gives rise to the need for systematic study of competing processes to understand and leverage the wide range of possible manganese oxide products. In the current work, nucleation of manganese oxide nanoparticles by gas-to-particle conversion is systematically examined.

Condensation of nanoparticles from the gas-phase is potentially limited by a thermodynamic barrier at high flame temperature and low precursor concentration. The Kelvin effect is used to quantify the thermodynamic barrier for conversion of gas-phase clusters to the condensed phase by accounting for the supersaturation of condensable species and the surface tension of the resulting particle or droplet [21]. Particle nucleation and growth occur immediately after the product is formed (coagulation-limited) if the size of the monomer molecule is greater than the critical cluster size, r*, given by the Kelvin equation [21,22]:

$$r^* = \frac{2\,\sigma_s v_1}{k_b\,T \ln S} \qquad \text{eq. 1}$$

where σ_s is the surface energy or tension of the cluster, v_1 is the molecular volume, k_B is Boltzmann's constant, T is the local temperature and S is the saturation ratio. This criterion has been applied to SiO_2 [9] and TiO_2 [23] particle formation to show that coagulation governs particle nucleation and, hence, the final particle size for flame synthesis conditions with high supersaturation of precursors. Our recent report [15] on manganese oxide synthesis in premixed stagnation flames provided evidence that the higher flame temperatures and ppm level of precursor doping may give rise to a thermodynamic

[a] *Mechanical Engineering Department, San Diego State University, San Diego, CA USA*
[b] *Mechanical and Aerospace Engineering Department, University of California San Diego, San Diego, CA, USA*

barrier for particle nucleation. The range of oxidation states observed made application of simple coagulation models less accurate due to the additional contribution of oxidation to particle size. The lowest oxidation state product, MnO, is the focus of the current work to enable isolated study of nucleation and growth in the absence of further oxidation steps.

The current work is a complementary experimental and modeling study of manganese oxide synthesis in premixed stagnation flames. The temperature-oxygen-time history of the particle is well-characterized during synthesis in premixed stagnation flames due to reliable numerical models of the flame structure. Thermodynamic analysis of the manganese-oxygen-manganese oxide system is applied for insight into equilibrium conditions based on the computed underlying flame structure. Measurements of the flame position and final particle size are used to evaluate assumptions of the flame structure computation and coagulation growth model.

Aerosol probe sampling is carried out here to analyze the particle size distribution of flame-formed particles in real-time by mobility sizing. An effective technique established for sampling soot from flames under well-characterized boundary conditions [24,25] is applied here to investigate nucleation of manganese oxide nanoparticles. A wide range of dilution probe techniques were previously reported to investigate flame synthesis processes and material properties starting from the straight-tube design of Ulrich [26]. Kasper applied aerosol sampling using a quartz probe to investigate TiO2 flame synthesis processes [27] and other designs such as water-cooled [28,29] and multi-stage dilution [30–34] quartz sampling probes have since been employed for a variety of flame studies. Experimental [35,36] and modeling [12,36] investigation of perturbations to the flame synthesis process due to probe sampling have indicated that precise characterization of process parameters and material properties requires consideration of probe effects. The premixed stagnation flames currently studied are probed by embedding a sampling orifice flush with the flat stagnation surface. This design enables probe sampling with more clearly defined effects on the flame structure caused by flow stagnation and suction.

Computational

Computations of the flame structure are carried out here without precursor chemistry or oxide particle formation processes. A well-known anti-knock agent, manganese methylcyclopentadienyl tricarbonyl (MMT), is fed into the premixed stagnation flames as a gas-phase precursor. Inhibition chemistry for MMT has been established by Linteris for methane flames [37,38] but the inhibition efficiency has been shown to be half as effective as iron pentacarbonyl with additional loss in inhibition for concentrations in which particles are formed. In addition, perturbation to the flame structure was not observed for premixed propane flames doped with MMT [39]. Our previous study [15] also showed comparable flame position between base ethylene-oxygen-argon flames and flames doped with MMT. These reported observations for propane and ethylene flames may indicate that inhibition is weaker for larger hydrocarbon flame chemistry. This comparison will also be carried out for the current flame to assess the performance of the base flame chemistry model in predicting the flame structure in the presence of MMT precursor.

The premixed stagnation flame (ethylene-oxygen-argon) is modeled here using both a pseudo one-dimensional formulation and a solution to the two-dimensional axisymmetric flow field. The pseudo one-dimensional (OPPDIF [40,41]) approach has been shown to provide fast and reasonably accurate solutions for the centerline profiles even for configurations having plate separation distance greater than the nozzle diameter [15]. The two-dimensional (ANSYS Workbench v. 19.2) formulation is used here to evaluate perturbations of the flow field due to aerosol probe sampling. Both computations incorporate the CHEMKIN framework [42] with the USC Mech II [43] combustion chemistry model to minimize differences in computed flame structure due to differences in flame chemistry and transport. The computations are similar to previous work [15] except for the addition of a sampling probe to the two-dimensional ANSYS computation. As will be discussed below, the sampling probe is simply an orifice at the centerline of an otherwise flat stagnation surface. This is modeled as a slit at the stagnation plate boundary centered on the axis of the two-dimensional axisymmetric domain. The flow velocity measured during dilution ratio calibration is set as a boundary condition at this face to assess the perturbation of aerosol sampling to the flame structure and growth time.

For the manganese-oxygen-manganese oxide system, the following process:

$$Mn(g) + ½\ O_2(g) \rightarrow MnO(s) \qquad \text{eq. 2}$$

is hypothesized here for nucleation of manganese oxide in flames. Insights into the gas-to-particle conversion of manganese oxide could be gained from high-temperature studies of the solid-to-gas process. Gas-phase Mn and MnO are reported upon vaporization of solid MnO in high-temperature mass spectroscopy studies [44,45] which indicates dissociation occurs upon entering the gas-phase. Other studies have confirmed the partial pressure of metallic Mn is orders of magnitude higher than MnO at elevated temperature [37,46]. Based on the reported stability of the high-temperature Mn-MnO-O_2 system, it follows that condensation of MnO occurs more readily than condensation of metallic Mn. The enthalpy of reaction for sublimation of solid MnO to the gas-phase has been reported at 532 kJ/mol while the dissociative sublimation (reverse of eq. 2) has been reported at 644 kJ/mol [46]. Combination of Mn and O2 to condense MnO can be considered more thermodynamically favored than condensation of gas-phase MnO based on the reported enthalpies of reaction. The breakdown and flame chemistry associated with the MMT precursor is complex. Linteris introduced gas-phase chemistry of Mn oxidation based on studies of MMT doped flames [37,38] but particle formation processes were not considered. Gas-to-particle conversion to manganese oxide is likely to stem from a variety of species to produce a range of initial particle types. A simple global model is applied here based on existing equilibrium parameters of the high-temperature Mn-MnO-O2 system and nano-scale manganese oxides. The oxygen-deficient flame condition chosen is designed to minimize contributions from higher oxidation states of manganese such that nucleation

and growth of MnO could be isolated. Errors associated by modeling nucleation and growth based on eq. 2 are counter-balanced with a well-characterized reaction environment and by narrowing the range of potential manganese oxide species. Improvement of the flame chemistry and aerosol models will be carried out in future work based on the global thermodynamic analysis carried out here.

High-temperature equilibrium partial pressures have been reported for this system from Knudsen effusion mass spectroscopy measurements [46] as follows:

$$\ln\left(\frac{P_{Mn,eq}}{pascal}\right) = \frac{-64{,}412}{T} + 35.668 \qquad \text{eq. 3}$$

$$\ln\left(\frac{P_{O2,eq}}{pascal}\right) = \frac{-27{,}064}{T} + 11.461 \qquad \text{eq. 4}$$

where $P_{Mn,eq}$ and $P_{O2,eq}$ are the equilibrium partial pressures of Mn and O_2 in Pascal. Local equilibrium partial pressures for Mn and O_2 are computed along the computed temperature profile for insight into supersaturation leading to manganese oxide condensation. In addition, the computed profiles are transformed from the space domain to a Lagrangian time profile using the computed axial convective and thermophoretic velocity [15,24,47]. Decomposition of MMT is expected to occur in the vicinity of the flame zone such that oxidation, nucleation and growth of manganese oxide nanoparticles is a one-dimensional progression in time from the flame zone to the stagnation surface. If particle nucleation occurs upon formation of MnO and no further oxidation occurs, particle growth will be determined by coagulation of MnO particles over time. The computed particle size is based on coagulation of like-sized particles starting from a monodisperse distribution of MnO monomers [21] as follows:

$$d(t_i) = d_{i-1}\left(1 + \frac{K_{ii}\, N_{i-1}\, t_{i-1}}{2}\right)^{1/3} \qquad \text{eq. 5}$$

where d is the particle size computed discretely from the computed temperature-time profile. A one-to-one proportion of MMT molecules to Mn atoms to MnO monomers is assumed and this gives the initial number density of monomers (MMT has a single Mn ligand). After each grid point denoted by time ti , growth occurs from the size at the previous grid point d_{i-1}. The number density at the previous grid point is N_{i-1} and the time interval from the previous grid point is t_{i-1}. K_{ii} is the coagulation coefficient of like-sized particles in the free-molecular regime:

$$K_{ii} = 4\alpha\left(\frac{6\, K_B\, T\, d_{i-1}}{\rho_P}\right)^{1/2} \qquad \text{eq. 6}$$

where α is the collision efficiency and ρp is the bulk density of MnO. Nucleation-sized particles have collision efficiency as low as ten percent [48] but precise values for the current system are unknown. As such, eq. 6 is computed for a range of collision efficiency to report feasible particle sizes for the given growth time.

Experimental

The experimental configuration centers on synthesis of manganese oxide nanoparticles in premixed stagnation flames. The setup is similar to previous studies [15,47] with key details briefly describe here. The base flame is 8.8 % ethylene, 17.5 % oxygen and 73.7 % argon by mole which is a fuel-rich mixture (Φ = 1.5) expected to produce MnO based on previous studies [15]. A jet of unburned gas issues from an aerodynamic nozzle with contours of the inner nozzle specified by Bergthorson [49] to induce a plug flow profile. The nozzle inner diameter is 1.0 cm and the wall thickness at the nozzle exit is 0.2 cm. The length of the burner inner conduit is several times the nozzle diameter to ensure fully developed laminar flow. The nozzle flow has a cold gas velocity of 315 cm/s and the temperature is 400 ± 20 K at the nozzle exit as indicated by a fine-wire Type K thermocouple. A steady, flat flame is stabilized in between the nozzle and the stagnation surface surrounded by a flow of shroud nitrogen gas issued from a channel concentric to the nozzle. Flow stagnation is induced by a water-cooled block configured to hold aluminum sample deposition plates or the aerosol sampling probe assembly described below.

Liquid MMT is fed into the fuel line by spraying into a 50 mL flow chamber via argon driven (1 LPM) glass nebulizer (Precision Glassblowing 500-70M). The chamber is close to ambient temperature to prevent clogging of the capillary as the nebulizer is rated for micro-flow (0.1 mL/min liquid flow) and 1 micron droplet size. The spray flows from the chamber to the heated fuel line (393 K) and mixes with the unburned mixture with a residence time of approximately 2 seconds before reaching the flame. The liquid flow is precisely regulated by syringe pump, but the uncertainty of the doping concentration is ± 10 % based on measurable liquid volume draining from the spray chamber walls after experiments. Precursor loading of 100, 250, 400, 550 and 800 ppm of vaporized MMT is examined but full analysis is only carried out for the 400 and 800 ppm conditions.

Aerosol sampling is carried out using a probe design similar to previous studies [24,47,50] modified by a significant increase in the probe orifice diameter. The probe assembly is a thin-wall (0.125 micron) stainless steel ¼ inch tube mounted into an aluminum plate such that the probe orifice is flush with the plate to form a flat stagnation surface. Previous designs incorporate micro-orifice sampling with orifice diameter on the order of 100 microns to minimize probe perturbation and residence time across the orifice [51]. The current orifice diameter is 800 microns to compensate for the limited access to the probe in the closed synthesis chamber. Particle deposits accumulate in the orifice over time and should be regularly cleaned for reproducible results. The larger orifice maximizes the time in between orifice cleanings but probe perturbations and probe induced artifacts become more difficult to avoid.

Analysis of the flame-formed aerosol is carried out in real-time by mobility particle sizing. The outlet of the probe assembly carrying the particle laden flow is fed through the front panel of the synthesis chamber through conductive tubing

(¼ inch inner diameter). The 50 cm tube length and 30 LPM sample flow correspond to approximately 30 ms before entering the mobility sizing system. A TSI 1 nm Scanning Mobility Particle Sizer (TSI 3838E77) consisting of a dual voltage classifier (TSI 08,202), a Kr-85 bi-polar diffusion charger (Neutralizer TSI 3077A), 1 nm differential mobility analyzer (DMA) (TSI 3086), a diethylene glycol-based (DEG) condensation particle counter (CPC) (so-called Nanoenhancer, TSI 3777) and a butanol-based CPC (TSI 3772) is used in the "compact" configuration recommended by the vendor to minimize diffusion loss of small particles. See previous work for more details and schematics of the mobility sizing setup [15]. TSI Aerosol Instrument Manager Software (version 10.2) is used to collect and export the measured particle size distribution functions (PSDFs). An insert supplied by the vendor is now mounted onto the inlet of the neutralizer to minimize flow recirculation for more predictable attainment of the equilibrium charge distribution. TSI also measured the penetration of ultra-fine particles through the system flow path recently and a new diffusion loss correction [52] is applied to the measured PSDF.

X-ray diffraction (XRD) and TEM analysis is carried out on a PANalytical X'pert Pro diffractometer and FEC Tecnai 12, respectively. Mn oxide nanoparticles condense in the flame and deposit onto the stagnation surface. The analyzed sample is a mesoporous film which grows on a deposition plate mounted flush with the water-cooled stagnation surface. The temperature of the film depends on the heat transfer to the water-cooling and the heat flux from the synthesis flame. Aluminum sample plates are used to enhance cooling heat transfer and the deposition time is minimized (~ 1 minute) to reduce artificial sintering of the delicate film by prolonged exposure to the flame. TEM samples are prepared by scaping this film from the deposition plate, suspending the loose particles in ethanol and drop casting the suspension onto holy carbon-copper TEM grids. The flame position is measured by analysis of images of flame projections obtained from a Nikon D5300 DSLR camera.

Results and discussion

Known equilibrium concentrations for the nucleation reaction (eq. 2) enables determination of the saturation ratio and Kelvin effect as a function of temperature. The saturation ratio for this process is given as:

$$S = \frac{P_{Mn}P_{O2}^{1/2}}{P_{Mn,eq}P_{O2,eq}^{1/2}} = K_P(t)P_{Mn}P_{O2}^{1/2} \quad \text{eq. 7}$$

where P_{Mn} and P_{O2} are the local concentrations. The initial partial pressure of Mn is given by the known MMT feed concentration assuming oxidation of manganese begins from Mn atoms produced by decomposition of MMT at a one-to-one ratio. Evaluation of the equilibrium constant and critical radius for the nucleation reaction is shown in Fig. 1 as a function of temperature. Relatively low precursor concentrations of MMT precursor and O_2 are evaluated to assess the Kelvin effect in flames with low precursor loading. Under these conditions, production of MnO(s) is not thermodynamically favored above 1800 K. Application of the critical radius criterion for the MnO molecular radius (r_{MnO} = 0.17 nm) indicates that condensation of MnO monomers is unstable above 2000 K even for fuel-lean flames ($P_{O2} = 10^{-1}$ atm).

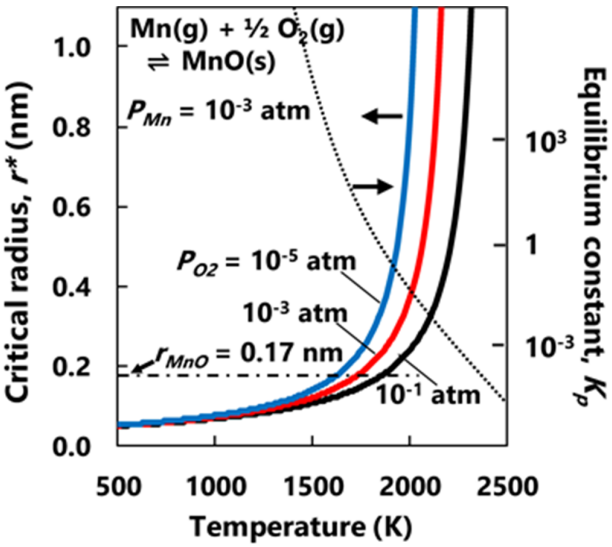

Figure 1. Critical Kelvin radius and equilibrium constant for the nucleation reaction as a function of temperature.

The effect of MMT precursor doping on the flame structure is assessed here in terms of the measured flame position. Images of flame projections for doped flames is compared to the base flame in Fig. 2. The flame standoff distances, Ls , reported in Fig. 2 are determined by analyzing the edges of the grey-scale intensity profiles for 30 flame images. Inspection of the images and reported standoff distances show no significant effect of MMT precursor loading on the flame position. The position of the flame zone is determined by the kinematic balance between the local flow velocity and the local burning velocity towards the unburned mixture [53]. As such, the flame structure is intimately coupled to the underlying flame chemistry for premixed stagnation flames. Any inhibition due to MMT is expected to cause a decrease in flame speed and/or a reduction in flame temperature. In turn, the flame is expected to respond by a shift in position due to a perturbation in the flame speed or temperature. Lack of this response may indicate that MMT inhibition chemistry is quenched by the formation of particles or the radical recombination processes established by Linteris [38] are less impactful for fuels larger than methane.

Computations of the flame structure are carried out using the pseudo one-dimensional formulation (OPPDIF) and solution to the two-dimensional axisymmetric flow field (ANSYS). Computed profiles at the centerline of the flame are compared to the experimental flame in terms of the measured grey-scale intensity recorded by the camera. For the base flame, the luminosity detected by the camera is assumed to be comparable to the excited radical CH* position and this comparison is shown in Fig. 3. The thin region of luminosity in premixed flat flames is due to chemiluminescence of excited radicals such as CH*, C2*, and OH* [54]. A previous report on fuel-rich premixed flames [55] showed that emission of CH* and C2* occurs in the same thin region in the flame zone. The comparison between computed CH* and measured intensity taken here is not make a conclusion of CH* production. Rather,

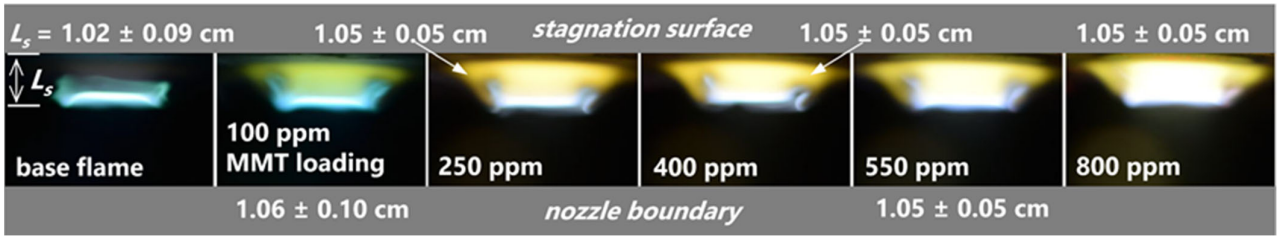

Figure 2. Flame images and measure flame standoff distances for the base flame and flames with increasing MMT loading.

the computed CH* is a marker in space for the computed narrow flame region of where excited flame radicals exist. The computed temperature profile is compared to the measured intensity for MMT doped flames in the bottom frame of Fig. 3. No inference is made here to measure the CH* or temperature values based on camera intensity. Rather, the comparison shown in Fig. 3 is only to quantify any differences in measured flame position. The relatively good agreement between the flame position inferred from OPPDIF, ANSYS and camera intensity is a basis for using the computed flame structure for analysis of nucleation and growth of MnO.

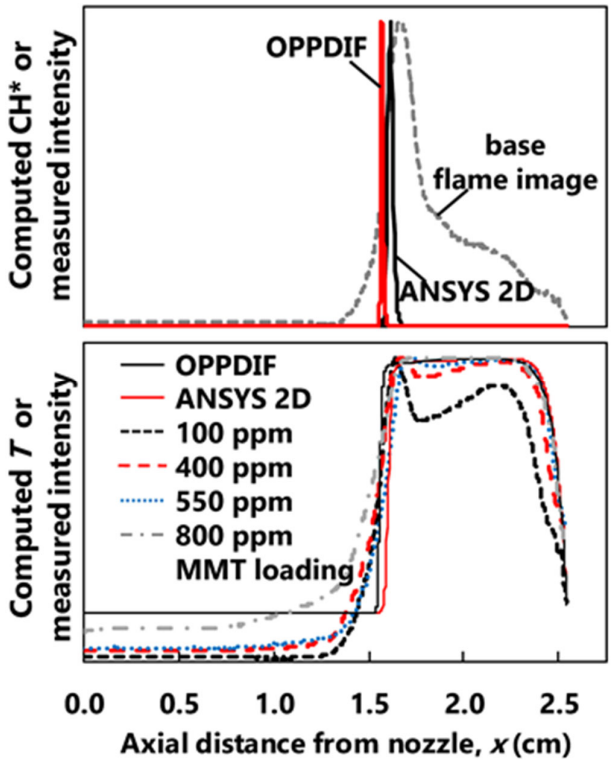

Figure 3. Computed centerline CH profile compared to measured grey-scale camera intensity from the base flame (top) and computed centerline temperature compared to measured grey-scale camera intensity for increasing MMT precursor loading (bottom).*

The particle size distribution of flame synthesize manganese oxide nanoparticles is measured here by mobility particle sizing and analysis of TEM images. Mobility sizing is a real-time measurement based on an aerosol sample pulled from the flame. The perturbation to the flame due to probe sampling is evaluated here by modeling the two-dimensional flame structure with a sampling flow applied to the stagnation surface boundary. The computed axial convective velocity and temperature contours are shown in Fig. 4 along with an image of a typical MMT doped flame. Without sampling suction, the convective velocity at the stagnation surface is zero due to the non-slip boundary condition and the temperature is assigned the measured value of the water-cooled surface (Tstag = 473 K). The flow rate into the orifice was measured, as discussed below, at various levels of suction. In Fig. 4, the flow velocity through the face of the sampling orifice is set to 200 cm/s to show the perturbation at the higher end of the experimentally applied suction. The computed profiles predict significant perturbations to the temperature and velocity field, but this effect is localized to a narrow region close to the sampling orifice. As expected, the flow induced by sampling suction increases the temperature of the flow entering the orifice.

The probe perturbation is further illustrated in Fig. 5 in terms of the computed centerline profiles of the two-dimensional solution. The solution for a 100 cm/s sample flow rate is also included to represent the flow rate range adopted for optimal sampling conditions. The axial convective flow velocity deviates from the stagnation flow solution approximately 1 mm upstream of the sampling orifice boundary. Manganese oxide nanoparticles present in the flame are assumed to follow gas streamlines except in the vicinity of the stagnation surface where an additional force on the particle induces a thermophoretic velocity towards the colder surface. The computed thermophoretic velocity, shown in Fig. 5, decreases significantly as probe induced flow makes the temperature gradient less severe compared to the stagnation flow solution. The reaction time computation shown in Fig. 5 is based on the sum of convective and thermophoretic velocities. The reaction time label is based on the assumption that the time for conversion of manganese oxide precursors to the final product begins at the flame zone and ends at the stagnation surface boundary. The flow induced by the probe sampling speeds up the particle more than reduction in thermophoretic velocity. Thus, the reaction time is significantly lower than the stagnation flow solution when probe perturbation is accounted for. For the 100 cm/s sample flow condition, the reaction time is reduced by 20% relative to the time computed for the stagnation flow. This magnitude of flow perturbation is on the same order as the perturbation reported for sampling probe perturbation in premixed burner-stabilized flames [56].

Analysis of the flame synthesized manganese oxide is carried out by XRD to characterize the oxide phase and structure. Diffraction patterns for films deposited from the 400 and 800 ppm MMT loading cases are shown in Fig. 6. Sintering during deposition is minimized by using aluminum substrates for efficient heat transfer from the water-cooled block. No

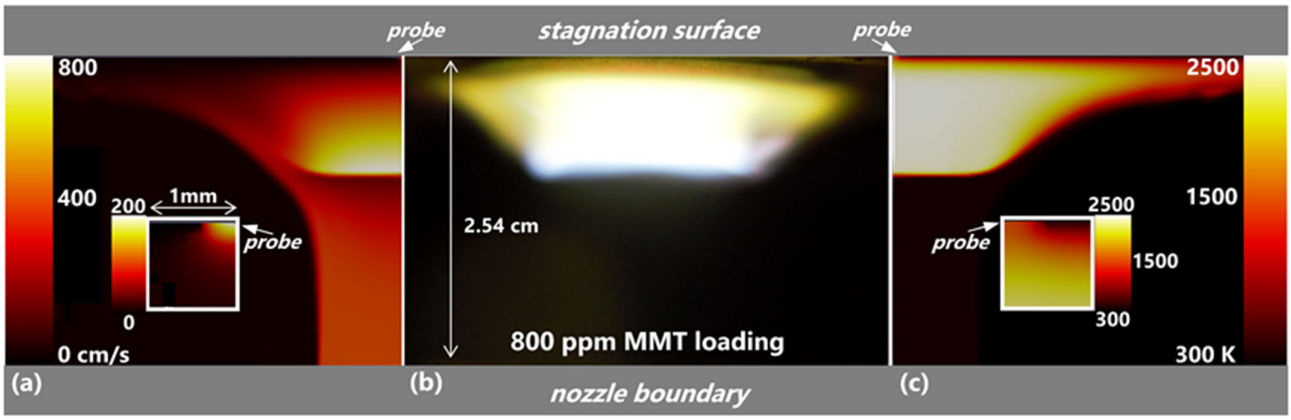

Figure 4. Computed axial velocity (a) and temperature (c) contours for the base flame with outflow through a sampling orifice (r = 0.4 mm) at the centerline axis. The inset of the computed contours shows the perturbations to the velocity and temperature field in a 1 mm by 1 mm domain at the sampling probe boundary. Also shown is an image for a typical flame doped with MMT precursor without sample suction (b).

significant diffraction was observed from samples deposited on aluminum which indicates that the film material is amorphous and/or any crystalline regions are very small. Faint evidence of the (200) face of MnO is observed for the as-deposited 800 ppm case but most of the signal an amorphous hump. A second deposition experiment was carried out using quartz deposition surfaces to inhibit heat transfer to the water-cooled block. This artificially induces sintering of the deposited film over the deposition period to provide an indication of the oxidation state of the flame synthesized product. Prominent, yet broad diffraction peaks corresponding to known MnO faces (JCPDS 07-0230) are observed after sintering is induced during deposition. Comparison of the relative intensities indicates that slight differences in stoichiometry may exist between the 400 and 800 ppm conditions. Nonetheless, the XRD analysis indicates that ultrafine particles with oxidation state at or close to MnO are produced. In the absence of significant oxidation beyond MnO, nucleation and growth processes could be examined in isolation.

Thermodynamic analysis along the computed temperature and gas-phase oxygen profiles is carried out to assess the Kelvin effect on MnO nucleation in the flame. The computed flame structure obtained by OPPDIF is shown in Fig. 7 in terms of the temperature and gas-phase oxygen as a function of reaction time. The reaction time is a Langrangian reference frame where the position of the flame zone is t = 0 and the final reaction time occurs upon reaching the stagnation surface. For coagulation-limited growth, particles would form at t = 0 and grow over the entire reaction time. Stretch-stabilized flames are relatively hot and this may introduce a condition in which condensation of MnO is not stable until the flame temperature decreases in the vicinity of the water-cooled stagnation surface. The OPPDIF stagnation flow solution is the basis of the thermodynamic analysis but the conclusions also apply to the probe perturbed conditions after shifts in time and temperature are taken into account. The current flame is fuel-rich but small amounts of gas-phase oxygen are predicted to remain in the post-flame region. The flame-zone is a very narrow region where the flame temperature quickly approaches the adiabatic flame temperature and this temperature persists through most of the post-flame region. On approach to the stagnation surface, the flame temperature approaches the temperature of the water-cooled surface. Any nanoparticles formed in the flame are assumed to follow the flow streamlines with exception to the cooling region where the thermophoretic force induces an additional particle velocity towards the stagnation surface.

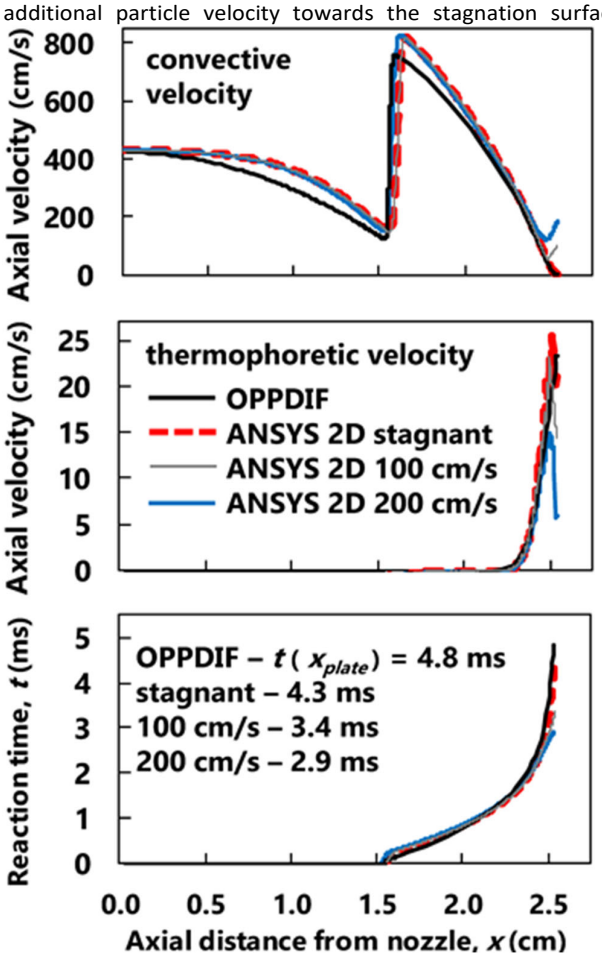

Figure 5. Computed centerline profiles of axial convective velocity (top), axial thermophoretic velocity (middle) and reaction time (bottom). Solutions for the stagnation flow is presented from OPPDIF and ANSYS along with the solution for sampling probe induced flows of 100 cm/s and 200 cm/s.

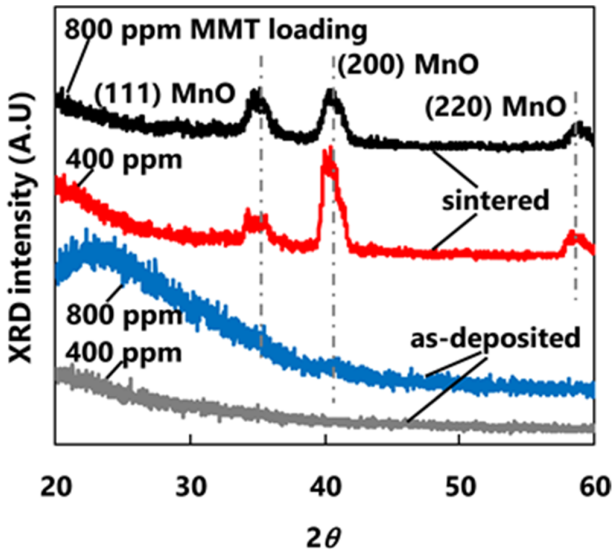

Figure 6. XRD patterns for as-deposited and sintered films deposited from the flame.

The basis of the thermodynamic analysis is that the local gas-phase Mn and O2 concentrations determine the saturation conditions according eq. 5-7. The saturation ratio profile for zero Mn converted is shown along with the profile for 99% conversion of Mn in Fig. 8 to represent the limiting cases for the gas-to-particle conversion. Within this range, supersaturation is only achieved as the flame temperature decreases significantly from the peak temperature of 2600 K. The saturation ratio is not sensitive to the factor of two difference between precursor loading cases. This is evident in the overlapping curves in the cooling region where S > 1. As Fig. 8 shows, the Kelvin equation is also insensitive to the precursor loading conditions. Computation of the critical Kelvin diameter based on the local saturation ratio indicates that condensation of MnO monomers become stable 3 to 4 ms after the flame zone for both 400 and 800 ppm MMT precursor loading conditions. In other words, a thermodynamic barrier may delay nucleation and growth of MnO nanoparticles for the current flame temperature and precursor conditions. The barrier may play a role in flame synthesis conditions at relatively high-temperature, low precursor loading and/or composite materials having a range of proportions. In the current work, this analysis is a factor in interpreting the particle size measured for particles collected at the stagnation surface.

Calibration of the aerosol sampling probe dilution is carried out by measuring the flow rate of air flowing into the probe orifice by bubble-flow meter (mini-Buck M-1) in a procedure described previously [25,51]. The dilution ratio calibration is shown in Fig. 9 as a function of indicated pressure drop across the orifice. The indicated pressure drop is the average pressure drop determined by monometers placed at the inlet and outlet of sampling probe tube. Reversal of the flow from positive to negative flow is observed as the average pressure drop approached 28 mm H2O. The measured flow rates correspond to sample flow velocities spanning 50 – 400 cm/s.

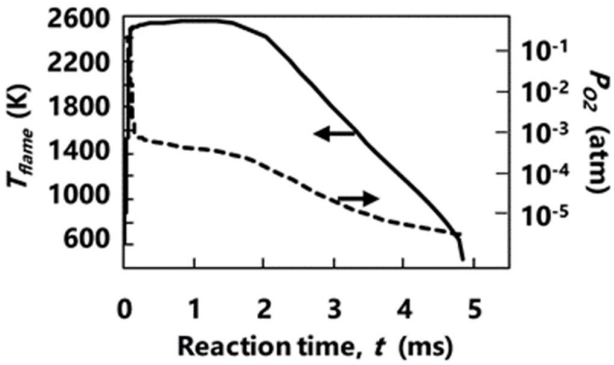

Figure 7. Temperature and oxygen as a function of reaction time determined by the pseudo-1D stagnation flow computation (OPPDIF).

The size distribution of the aerosol sample is measured by mobility sizing for a range of dilution ratio (probe suction) to assess artificial perturbations. For low sample dilution, the relatively high number density undergoes rapid coagulation growth across the sampling orifice causing an artificial drop in number density and increase in median diameter. For high dilution, the relatively long residence time across the orifice allows for significant diffusion loss of small particles to the wall. Ideally, an optimum range of dilution ratio exists where the dilution corrected number density and median diameter are insensitive to the applied dilution [51]. Sampling artifacts to the measured PSDF are minimized in this optimal region.

Each measured PSDF is fit to a log-normal distribution to obtain the number density, median mobility diameter and geometric standard deviation. Measured PSDF number density and median diameter for the 400 ppm MMT loading condition, shown in Fig. 10, indicates that the optimal sampling dilution range is narrow. Namely, a peak in the dilution corrected number density occurs around 200 dilution ratio and the median diameter is close to 4 nm within this dilution ratio range. The measured values are the average of 8-10 separate scans (30 second scan of DMA voltages for 1 to 20 nm mobility diameter) with error bars representing typical deviation across runs. The median mobility diameter and number density are determined to be 4 ± 1 nm and (2 ± 1) x1011 cm-3 for the 400 ppm loading case based on conservative interpretation of the response of the PSDF to dilution ratio.

This measurement is also reported in Fig. 11 for the 800 ppm MMT loading condition. The optimal region where the PSDF number density and median diameter is clearer for the 800 ppm case. The median mobility diameter and number density are determined to be 5.5 ± 1 nm and (6 ± 1) x1011 cm-3 based on interpretation of the response of the PSDF to dilution ratio. Dilution corrected PSDF are shown in Fig. 12 for the 400 and 800 ppm MMT loading conditions. Deviations in the PSDF are due to minor fluctuations in the flame and sampling conditions across and during scanning periods. These fluctuations include drift of the applied pressure drop and deposit accumulation at the sampling orifice. The observed increase in median diameter and geometric standard deviation provide insight into the underlying aerosol growth processes. Significant diffusional losses in the sampling line exist at the inlet valve and tubing where the flow splits and slows down in the final 10 cm before entering the mobility analyzer.

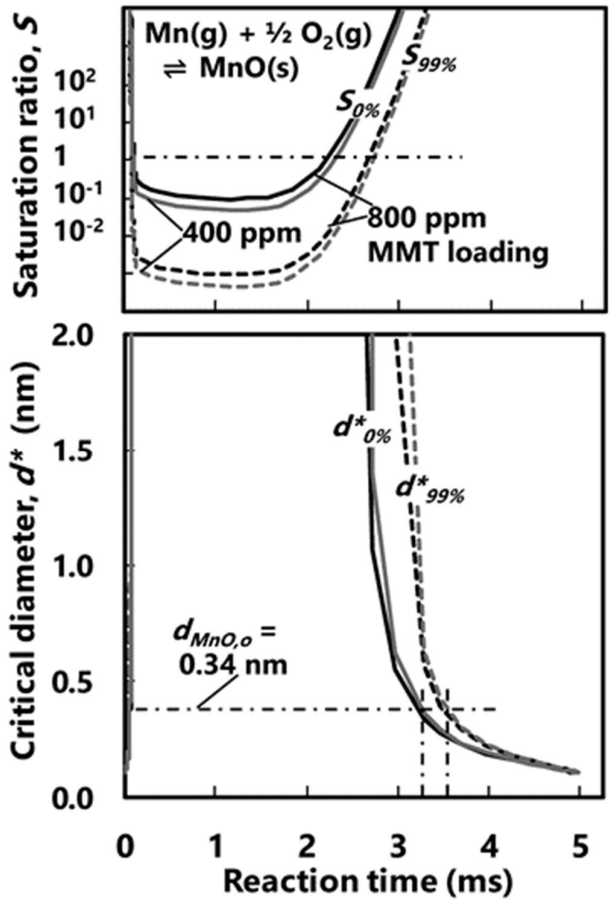

Figure 8. Thermodynamic analysis for MnO nucleation in terms of the saturation ratio (top) and critical Kelvin diameter (bottom) based on computed temperature and oxygen profiles.

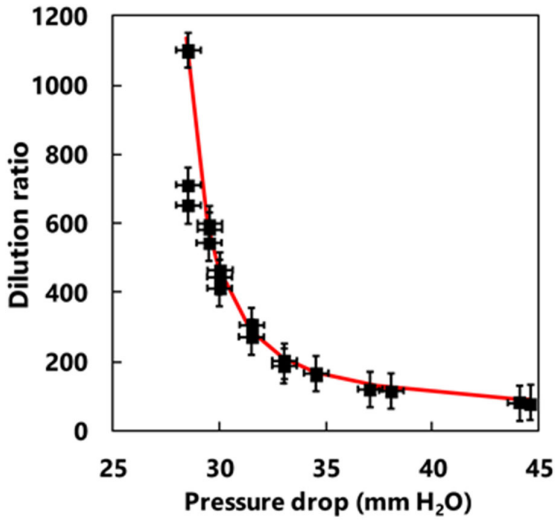

Figure 9. Measured dilution ratio calibration in terms of the indicated pressure drop across the sampling orifice.

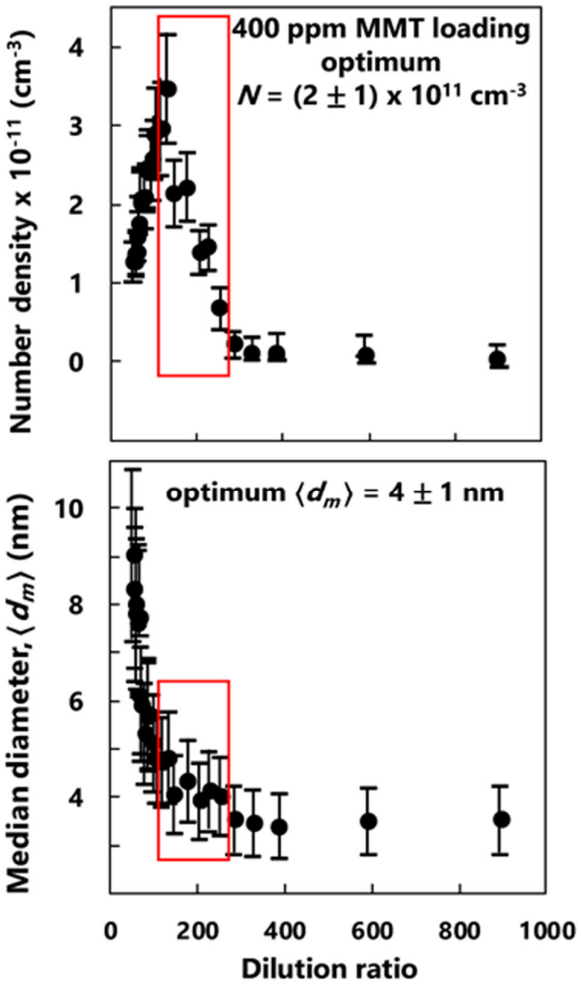

Figure 10. Measured PSDF number density and median diameter for the 400 ppm MMT loading condition for a range of sample dilution ratios.

The particle size distribution is also measured by analyzing TEM images for the 400 ppm and 800 ppm MMT loading cases. The sample particles correspond to the "as-deposited" case shown in the XRD patterns which was obtained by depositing onto an aluminum substrate to minimize sintering. Example TEM images and the distribution of measured projection diameters are shown in Fig. 13. The histogram is a distribution for a total of 150 particles for each ppm loading case. The median diameter determined by TEM is in reasonable agreement with the mobility diameter-based distributions. The observed ultrafine size is also in line with the lack of XRD signal observed for the as-deposited films. The particle size measured by mobility sizing and TEM corresponds to the end of the particle growth process. Gas-to-particle conversion occurs at some point upstream of the stagnation surface and measurement of the particle size at the stagnation boundary provides insight into the underlying nucleation and growth mechanisms in the flame. The measured particle sizes provide an experimental comparison to the particle size predicted from the gas-phase flame temperature-time profile.

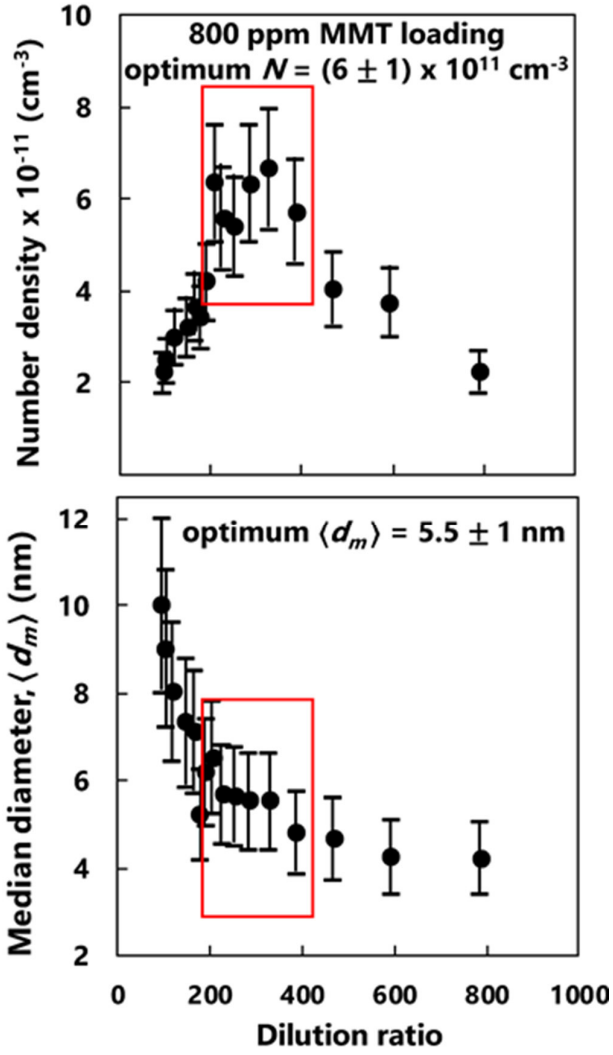

Figure 11. Measured PSDF number density and median diameter for the 800 ppm MMT loading condition for a range of sample dilution ratios.

The temperature-oxygen-time history of the particle during growth in flame can be inferred from the computed flame structure. Moreover, analysis of the thermodynamic barrier provides insight into the time at which nucleation becomes stable. If a thermodynamic barrier for nucleation is present, the observed particle size would be smaller due to the delay in particle condensation and growth. This hypothesis is tested in Fig. 14 in terms of particle size profiles computed as a function of reaction time. Comparison of expected particle size for coagulation-limited and nucleation-limited regimes is done by application of the monodisperse coagulation rate expression starting from the position of the flame zone (t = 0) and at a downstream position determined by the critical Kelvin diameter.

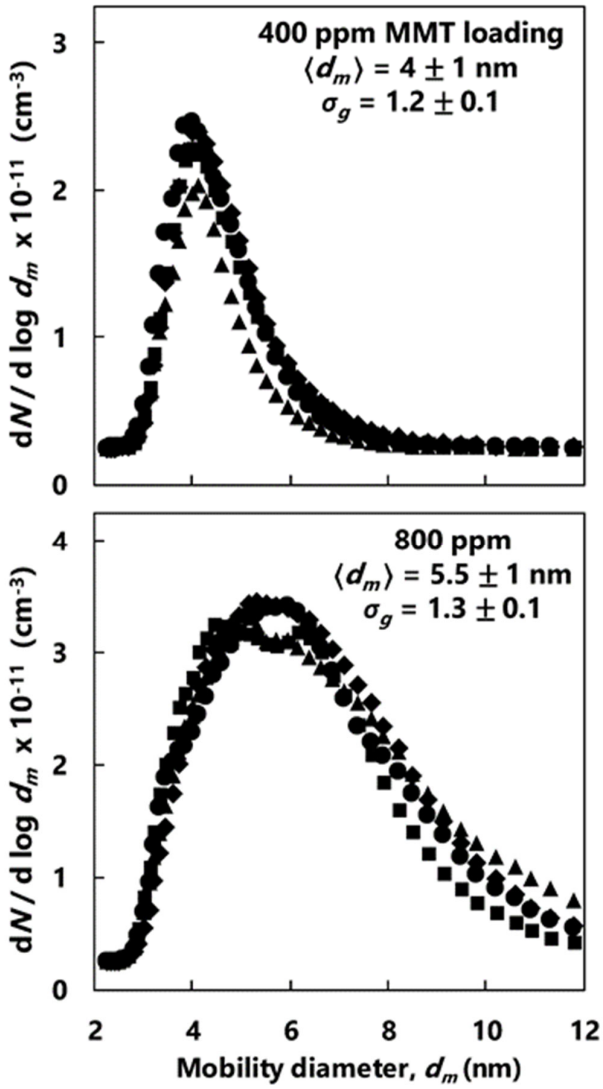

Figure 12. Measured PSDF at optimal sampling conditions for the 400 ppm (top) and 800 ppm MMT loading (bottom) cases. Different symbols are used to denote separate experimental runs which correspond to the optimal range of dilution ratio specified in Fig. 10 and Fig. 11.

Nucleation from MnO monomers is predicted to occur over 3 ms after the flame zone for both 400 ppm and 800 ppm levels of precursor loading based on the critical diameter criterion. Assuming a constant collision efficiency of α = 0.65, the final particle size computed for the nucleation limited regime is 4.8 and 5.9 nm for the 400 and 800 ppm cases, respectively. Computations are also shown for α = 0.3 and 0.9 to represent the range of feasible particle sizes resulting from coagulation growth. The computed particle size is nearly double for coagulation limited growth. The measured particle size is much closer to the size predicted for the nucleation-limited regime for both the 400 ppm and 800 ppm loading cases. The mobility diameter is subject to uncertainty in the growth time induced by flow perturbation. However, the size measured by TEM

indicates that the particle size is not significantly higher under full stagnation flow conditions. The applied sample suction amounts to 20% faster reaction time which roughly accounts for the discrepancy between the size measurement techniques. Excessive suction was not applied, but Fig. 14 labels the reaction time computed for the lowest dilution ratio case to demonstrate that the coagulation-limited growth regime does not explain the relatively small particle size observed. The smaller than expected particle size is evidence that the current temperature and precursor conditions do not induce high-levels of supersaturation and the Kelvin effect may hinder nucleation.

The current analysis is subject several assumptions and experimental uncertainties, but the results are conclusive in terms of observation of particle sizes significantly lower than predictions of coagulation-limited growth. Disappearance of nucleated particles at elevated temperatures has been reported for iron oxide synthesis in premixed flat flames [36] and TiO2 production in turbulent flow reactors [23] but this effect is more pronounced in premixed stagnation flames due to flame stabilization at relatively high temperature. Isolated study of nucleation behavior carried out here for the manganese oxide system is invaluable for elucidating competing thermodynamic and kinetic processes leading to the wide-range of manganese oxides obtainable by flame synthesis.

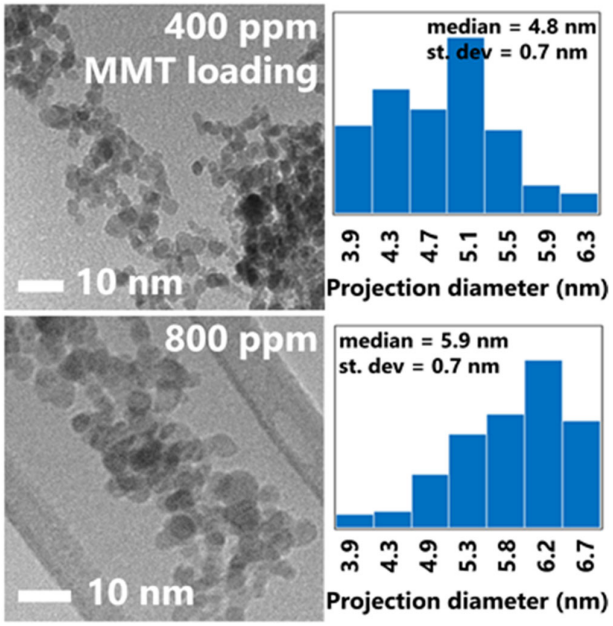

Figure 13. TEM images and particle size counts for the 400 ppm (top) and 800 ppm (bottom) MMT precursor loading conditions.

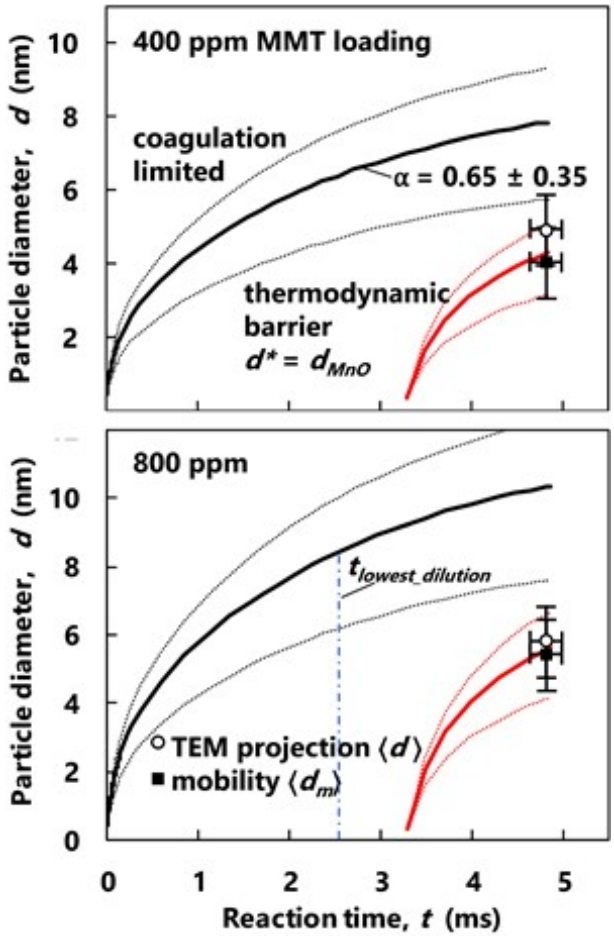

Figure 14. Computed particle diameter profile for the 400 ppm (top) and 800 ppm (bottom) MMT precursor loading conditions for coagulation limited growth and growth limited by a thermodynamic barrier. Also included are particle sizes measured by mobility sizing and TEM projections.

Conclusions

A complementary experimental and modeling study is reported here for nucleation of manganese oxide nanoparticles in premixed stagnation flames. The current flame synthesis occurs at relatively high temperature and precursor loading. Thermodynamic analysis based on the postulated nucleation process, Mn(g) + O2(g) → MnO(s), is carried out to quantify precursor supersaturation and potential barriers to nucleation. The computed temperature-time-oxygen history is the basis used to analyze nucleation and growth. The effect of MMT on the flame chemistry is assessed by comparing measured flame position for the base flame to flames having precursor loading from 100 ppm to 800 ppm. Measured flame standoff distances are unchanged relative to the base flame when MMT is added. This may indicate that the established inhibition flame chemistry is quenched by particle formation or less impactful for the fuels larger than methane. The measured flame position is also in agreement with flame position predicted by pseudo one-dimensional and two-dimensional solutions of the flame

structure. Agreement between measured and computed flame position is justification for basing the thermodynamic analysis on the computed flame structure.

Mobility particle sizing is carried out by aerosol sampling with probe perturbations characterized by two-dimensional flame structure computations including probe suction. Probe induced flow decreases the reaction time in the post-flame region by 20% compared to full stagnation flow. The observed discrepancy between median sizes measured by mobility sizing and TEM imaging may be due to differences in growth time. Thermodynamic analysis indicates that a thermodynamic barrier, quantified by the Kelvin effect, delays condensation of MnO for the flame synthesis conditions currently studied. The nucleation-limited growth mechanism explains the observed particle size much closer than growth predicted from a coagulation growth mechanism, even when probe perturbations are accounted for. Isolated study of nucleation behavior carried out here for the manganese oxide system is invaluable for elucidating competing thermodynamic and kinetic processes leading to the wide-range of manganese oxides obtainable by flame synthesis. In addition, supersaturation should be examined for gas-phase processes producing composite materials having a range in proportions.

Conflicts of interest

There are no conflicts to declare

Acknowledgements

The work was supported by NSF Combustion and Fire Systems program under Award 1841357. Prof. David Pullman (SDSU Chemistry) and Dr. Ingrid Neisman (SDSU Microscopy Center) are gratefully acknowledged for assistance in nanoparticle characterization.

References

[1] G.D. Ulrich, Special Report: Flame-generated fine particles, Chem. Eng. News Arch. 62 (1984) 22–29. https://doi.org/10.1021/cen-v062n032.p022.

[2] G.A. Kelesidis, E. Goudeli, S.E. Pratsinis, Flame synthesis of functional nanostructured materials and devices: Surface growth and aggregation, Proc. Combust. Inst. 36 (2017) 29–50. https://doi.org/https://doi.org/10.1016/j.proci.2016.08.078.

[3] S. Li, Y. Ren, P. Biswas, S.D. Tse, Flame aerosol synthesis of nanostructured materials and functional devices: Processing, modeling, and diagnostics, Prog. Energy Combust. Sci. 55 (2016) 1–59. https://doi.org/https://doi.org/10.1016/j.pecs.2016.04.002.

[4] R.L. Vander Wal, L.J. Hall, Flame synthesis of Fe catalyzed single-walled carbon nanotubes and Ni catalyzed nanofibers: growth mechanisms and consequences, Chem. Phys. Lett. 349 (2001) 178–184. https://doi.org/https://doi.org/10.1016/S0009-2614(01)01198-8.

[5] N.K. Memon, S.D. Tse, J.F. Al-Sharab, H. Yamaguchi, A.-M.B. Goncalves, B.H. Kear, Y. Jaluria, E.Y. Andrei, M. Chhowalla, Flame synthesis of graphene films in open environments, Carbon N. Y. 49 (2011) 5064–5070. https://doi.org/https://doi.org/10.1016/j.carbon.2011.07.024.

[6] A. Münzer, L. Xiao, Y.H. Sehlleier, C. Schulz, H. Wiggers, All gas-phase synthesis of graphene: Characterization and its utilization for silicon-based lithium-ion batteries, Electrochim. Acta. 272 (2018) 52–59. https://doi.org/https://doi.org/10.1016/j.electacta.2018.03.137.

[7] R.L. Axelbaum, S.M.L. Sastry, D.P. Dufaux, C.A. Frey, A flame process for synthesis of unagglomerated, low-oxygen nanoparticles: Application to Ti and TiB2, Metall. Mater. Trans. B. 28 (1997) 1199–1211. https://doi.org/10.1007/s11663-997-0076-5.

[8] A.D. Abid, G. Smith, M. Krause, A. Yin, C. Sungail, Gas Phase Sodium Flame Synthesis of Non-Oxide Metallic Powder, TechConnect Briefs. (2018) 74–77.

[9] G.D. Ulrich, Theory of Particle Formation and Growth in Oxide Synthesis Flames, Combust. Sci. Technol. 4 (1971) 47–57. https://doi.org/10.1080/00102207108952471.

[10] S.E. Pratsinis, Flame aerosol synthesis of ceramic powders, Prog. Energy Combust. Sci. 24 (1998) 197–219. https://doi.org/https://doi.org/10.1016/S0360-1285(97)00028-2.

[11] T.P. Huelser, A. Lorke, P. Ifeacho, H. Wiggers, C. Schulz, Core and grain boundary sensitivity of tungsten-oxide sensor devices by molecular beam assisted particle deposition, J. Appl. Phys. 102 (2007) 124305. https://doi.org/10.1063/1.2817612.

[12] J. Sellmann, I. Rahinov, S. Kluge, H. Jünger, A. Fomin, S. Cheskis, C. Schulz, H. Wiggers, A. Kempf, I. Wlokas, Detailed simulation of iron oxide nanoparticle forming flames: Buoyancy and probe effects, Proc. Combust. Inst. 37 (2019) 1241–1248. https://doi.org/https://doi.org/10.1016/j.proci.2018.06.041.

[13] C. Liu, J. Camacho, H. Wang, Phase Equilibrium of TiO2 Nanocrystals in Flame-Assisted Chemical Vapor Deposition, ChemPhysChem. 19 (2018) 180–186. https://doi.org/10.1002/cphc.201700962.

[14] S. Memarzadeh, E.D. Tolmachoff, D.J. Phares, H. Wang, Properties of nanocrystalline TiO2 synthesized in premixed flames stabilized on a rotating surface, Proc. Combust. Inst. 33 (2011) 1917–1924. https://doi.org/http://dx.doi.org/10.1016/j.proci.2010.05.065.

[15] S. Dasappa, J. Camacho, Formation of nanocrystalline manganese oxide in flames: oxide phase governed by classical nucleation and size-dependent equilibria, CrystEngComm. 22 (2020) 5509–5521. https://doi.org/10.1039/D0CE00734J.

[16] J. Camacho, C. Liu, N. Montes, H. Wang, Ultrafine Manganese Oxide Nanoparticles Synthesized by Flame Stabilized on a Rotating Surface, 9th U. S. Natl. Combust. Meet. (2015) 2B09.

[17] E. Meeks, R.J. Kee, D.S. Dandy, M.E. Coltrin, Computational simulation of diamond chemical vapor deposition in premixed C2H2/O2/H2 and CH4O2-strained flames, Combust. Flame. 92 (1993) 144–160.

https://doi.org/http://dx.doi.org/10.1016/0010-2180(93)90204-G.

[18] J. Shin, R.M. Anisur, M.K. Ko, G.H. Im, J.H. Lee, I.S. Lee, Hollow Manganese Oxide Nanoparticles as Multifunctional Agents for Magnetic Resonance Imaging and Drug Delivery, Angew. Chemie Int. Ed. 48 (2009) 321–324. https://doi.org/10.1002/anie.200802323.

[19] M. Wiechen, M.M. Najafpour, S.I. Allakhverdiev, L. Spiccia, Water oxidation catalysis by manganese oxides: learning from evolution, Energy Environ. Sci. 7 (2014) 2203–2212. https://doi.org/10.1039/C4EE00681J.

[20] W. Wei, X. Cui, W. Chen, D.G. Ivey, Manganese oxide-based materials as electrochemical supercapacitor electrodes, Chem. Soc. Rev. 40 (2011) 1697–1721. https://doi.org/10.1039/c0cs00127a.

[21] S.K. Friedlander, Smoke, Dust, and Haze: Fundamentals of Aerosol Behavior, Oxford University Press, New York, 2000.

[22] A. Gurav, T. Kodas, T. Pluym, Y. Xiong, Aerosol Processing of Materials, Aerosol Sci. Technol. 19 (1993) 411–452. https://doi.org/10.1080/02786829308959650.

[23] Y. Xiong, S.E. Pratsinis, Gas phase production of particles in reactive turbulent flows, J. Aerosol Sci. 22 (1991) 637–655. https://doi.org/https://doi.org/10.1016/0021-8502(91)90017-C.

[24] A.D. Abid, J. Camacho, D.A. Sheen, H. Wang, Quantitative measurement of soot particle size distribution in premixed flames - The burner-stabilized stagnation flame approach, Combust. Flame. 156 (2009) 1862–1870.

[25] J. Camacho, C. Liu, C. Gu, H. Lin, Z. Huang, Q. Tang, X. You, C. Saggese, Y. Li, H. Jung, L. Deng, I. Wlokas, H. Wang, Mobility size and mass of nascent soot particles in a benchmark premixed ethylene flame, Combust. Flame. 162 (2015). https://doi.org/10.1016/j.combustflame.2015.07.018.

[26] G.D. Ulrich, B.A. Milnes, N.S. Subramanian, Particle Growth in Flames. II: Experimental Results for Silica Particles, Combust. Sci. Technol. 14 (1976) 243–249. https://doi.org/10.1080/00102207608547532.

[27] M. Katzer, A.P. Weber, G. Kasper, The effects of electrical fields on growth of titania particles formed in a CH4–O2 diffusion flame, J. Aerosol Sci. 32 (2001) 1045–1067. https://doi.org/https://doi.org/10.1016/S0021-8502(01)00041-6.

[28] P.S. Fennell, J.S. Dennis, A.N. Hayhurst, The sampling of nanoparticles of MgO formed when doping an oxygen-rich flame with magnesium: The measurement of the concentrations and size-distributions of these nanoparticles, Combust. Flame. 151 (2007) 560–572. https://doi.org/https://doi.org/10.1016/j.combustflame.2007.07.004.

[29] P.S. Fennell, J.S. Dennis, A.N. Hayhurst, The size distributions of nanoparticles of the oxides of Mg, Ba and Al in flames: Their measurement and dependence on the concentrations of free radicals in the flame, Proc. Combust. Inst. 31 (2007) 1939–1945. https://doi.org/https://doi.org/10.1016/j.proci.2006.07.137.

[30] H. Zhao, X. Liu, S.D. Tse, Effects of pressure and precursor loading in the flame synthesis of titania nanoparticles, J. Aerosol Sci. 40 (2009) 919–937. https://doi.org/https://doi.org/10.1016/j.jaerosci.2009.07.004.

[31] K.H. Ahn, S.H. Sohn, C.H. Jung, M. Choi, In situ measurement of nano particle size distribution and charge characteristics in H2/O2/TEOS diffusion flame, Scr. Mater. 44 (2001) 1889–1892. https://doi.org/https://doi.org/10.1016/S1359-6462(01)00806-5.

[32] K.H. Ahn, C.H. Jung, M. Choi, J.S. Lee, Particle Sampling and Real Time Size Distribution Measurement in H2/O2/TEOS Diffusion Flame, J. Nanoparticle Res. 3 (2001) 161–170. https://doi.org/10.1023/A:1017942805637.

[33] Y. Wang, J. Fang, M. Attoui, T.S. Chadha, W.-N. Wang, P. Biswas, Application of Half Mini DMA for sub 2nm particle size distribution measurement in an electrospray and a flame aerosol reactor, J. Aerosol Sci. 71 (2014) 52–64. https://doi.org/https://doi.org/10.1016/j.jaerosci.2014.01.007.

[34] N. Reed, J. Fang, S. Chavalmane, P. Biswas, Real-time measurement of size-resolved elemental composition ratio for flame synthesized composite nanoparticle aggregates using a tandem SMPS-ICP-OES, Aerosol Sci. Technol. 51 (2017) 311–316. https://doi.org/10.1080/02786826.2016.1271110.

[35] E. Goudeli, A.J. Gröhn, S.E. Pratsinis, Sampling and dilution of nanoparticles at high temperature, Aerosol Sci. Technol. 50 (2016) 591–604. https://doi.org/10.1080/02786826.2016.1168922.

[36] S. Kluge, L. Deng, O. Feroughi, F. Schneider, M. Poliak, A. Fomin, V. Tsionsky, S. Cheskis, I. Wlokas, I. Rahinov, T. Dreier, A. Kempf, H. Wiggers, C. Schulz, Initial reaction steps during flame synthesis of iron-oxide nanoparticles, CrystEngComm. 17 (2015) 6930–6939. https://doi.org/10.1039/C5CE00456J.

[37] G.T. Linteris, V.D. Knyazev, V.I. Babushok, Premixed flame inhibition by manganese and tin compounds, Halon Options Tech. Work. Conf. (2001) 72–86.

[38] G.T. Linteris, V.D. Knyazev, V.I. Babushok, Inhibition of premixed methane flames by manganese and tin compounds† †Official contribution of NIST, not subject to copyright in the United States, Combust. Flame. 129 (2002) 221–238. https://doi.org/https://doi.org/10.1016/S0010-2180(02)00346-2.

[39] U. Westblom, F. Fernandez-Alonso, C.R. Mahon, G.P. Smith, J.B. Jeffries, D.R. Crosley, Laser-induced fluorescence diagnostics of a propane/air flame with a manganese fuel additive, Combust. Flame. 99 (1994) 261–268. https://doi.org/https://doi.org/10.1016/0010-2180(94)90130-9.

[40] A.E. Lutz, R.J. Kee, J.F. Grcar, F.M. Rupley, OPPDIF: A Fortan program for computing opposed-flow diffusion flames, (1997).

[41] R.J. Kee, J.A. Miller, G.H. Evans, G. Dixon-Lewis, A computational model of the structure and extinction of strained, opposed flow, premixed methane-air flames, Symp. Combust. 22 (1989) 1479–1494. https://doi.org/http://dx.doi.org/10.1016/S0082-0784(89)80158-4.

[42] R.J. Kee, F.M. Rupley, J.A. Miller, Chemkin-II: A Fortran chemical kinetics package for the analysis of gas-phase chemical kinetics, (1989).

[43] H. Wang, X. You, A. V Joshi, S.G. Davis, A. Laskin, F. Egolfopoulos, C.K. Law, USC Mech II. High-Temperature Combustion Reaction Model of H2/CO/C1-C4 Compounds, Http://Ignis.Usc.Edu/USC_Mech_II.Htm. (2007).

[44] D.L. Hildenbrand, K.H. Lau, Thermochemistry of gaseous manganese oxides and hydroxides, J. Chem. Phys. 100 (1994) 8377–8380. https://doi.org/10.1063/1.466783.

[45] J.. Kazenas, W.. Tagirov, G.. Zviadatse, Mass spectrometric investigation of dissociation and sublimation of manganese oxide, Metally. 5 (1984) 58–59.

[46] A. Matraszek, M. Miller, L. Singheiser, K. Hilpert, Thermodynamic vaporization studies of the manganese oxide–yttria stabilized zirconia (YSZ) solid solution, J. Eur. Ceram. Soc. 24 (2004) 2649–2656. https://doi.org/https://doi.org/10.1016/j.jeurceramsoc.2003.09.015.

[47] J. Bonpua, Y. Yagües, A. Aleshin, S. Dasappa, J. Camacho, Flame temperature effect on sp2 bonds on nascent carbon nanoparticles formed in premixed flames (T > 2100 K): A Raman spectroscopy and particle mobility sizing study, Proc. Combust. Inst. 37 (2019) 943–951. https://doi.org/10.1016/j.proci.2018.06.124.

[48] N.A. Fuchs, Mechanics of Aerosols, Pergamon, 1964.

[49] J.M. Bergthorson, Experiments and Modeling of Impinging Jets and Premixed Hydrocarbon Stagnation Flames, California Institute of Technology, 2005.

[50] J. Camacho, A. V. Singh, W. Wang, R. Shan, E.K.Y. Yapp, D. Chen, M. Kraft, H. Wang, Soot particle size distributions in premixed stretch-stabilized flat ethylene-oxygen-argon flames, Proc. Combust. Inst. 36 (2017) 1001–1009. https://doi.org/10.1016/j.proci.2016.06.170.

[51] B. Zhao, Z. Yang, J. Wang, M. V Johnston, H. Wang, Analysis of Soot Nanoparticles in a Laminar Premixed Ethylene Flame by Scanning Mobility Particle Sizer, Aerosol Sci. Technol. 37 (2003) 611–620. https://doi.org/10.1080/02786820300908.

[52] TSI, Diffusion correction using TSI's 1 nm SMPS SYSTEM Model 3938, Application note SMPS-010 (US), 2019.

[53] C.K. Law, Combustion Physics, Cambrige Press, Cambridge, 2006.

[54] A.G. Gaydon, H.G. Wolfhard, Flames: Their Structure, Radiation, and Temperature, Chapman & Hall, 1979.

[55] J. Kojima, Y. Ikeda, T. Nakajima, Spatially resolved measurement of OH*, CH*, and C2* chemiluminescence in the reaction zone of laminar methane/air premixed flames, Proc. Combust. Inst. 28 (2000) 1757–1764. https://doi.org/https://doi.org/10.1016/S0082-0784(00)80577-9.

[56] C. Saggese, A. Cuoci, A. Frassoldati, S. Ferrario, J. Camacho, H. Wang, T. Faravelli, Probe effects in soot sampling from a burner-stabilized stagnation flame, Combust. Flame. 167 (2016). https://doi.org/10.1016/j.combustflame.2016.02.013.